NOTES AND CORRESPONDENCE

The Forced and Intrinsic Low-Frequency Modes in the North Pacific*

SOON-IL AN AND BIN WANG

International Pacific Research Center, SOEST, University of Hawaii at Manoa, Honolulu, Hawaii

(Manuscript received 4 November 2003, in final form 30 July 2004)

ABSTRACT

Conditional maximum covariance analysis is applied to investigate the coherent patterns between the tropical and North Pacific SST and the North Pacific 500-hPa geopotential height anomalies. Two leading modes are identified. One is an intrinsic midlatitude mode, the North Pacific (NP) mode, for which SST anomalies are mainly confined to the extratropical North Pacific. The other is a tropical ocean–atmosphere coupled mode, the ENSO mode, in which an ENSO-like SST pattern dominates the Tropics but extratropical SST anomalies are relatively weak.

The NP and ENSO modes exhibit distinct spatial and temporal characteristics. For the NP mode, atmospheric variation leads to changes in SST, while for the ENSO mode the opposite is true. The NP mode displays a persistence barrier during August–September whereas the ENSO mode has a March–April persistence barrier. The upper-tropospheric jet stream associated with the NP and ENSO mode intensifies, respectively, over the central North Pacific and the subtropical northeastern Pacific; consequently, the transient activities maximize in their corresponding jet exit regions. The expansion coefficients of the 500-hPa geopotential height associated with the two modes appear to be significantly correlated. However, by reducing the high-frequency part (e.g., shorter than the interannual time scale) in expansion coefficients, the correlation becomes insignificant, indicating that the significant correlation results from high-frequency signals that are unrelated to the corresponding SST variation. The results presented here suggest that the intrinsic coupled mode in the midlatitude North Pacific may be distinguished from the forced mode by remote ENSO, especially on the interannual time scale.

1. Introduction

The low-frequency, midlatitude atmospheric circulation anomalies are characterized by a geographically elongated pattern such as the Pacific–North American (PNA) and North Atlantic patterns (Wallace and Gutzler 1981). The PNA pattern is described as a wave train with a north–south dipole pattern in the central North Pacific. This pattern is somewhat reminiscent of the North Pacific Oscillation pattern found by Walker and Bliss (1932) and Bjerknes (1969). The North Pacific dipole extends farther downstream to North America with centers of action over western Canada and the southeastern United States. The PNA has been interpreted as forced by the El Niño–Southern Oscillation (ENSO) via atmospheric teleconnections (e.g., Horel and Wallace 1981; Graham 1994). This dynamic link between the extratropical circulation and tropical heat source was simply explained in a way of a linear Rossby wave ray-path theory (Hoskins and Karoly 1981). The atmospheric general circulation model (AGCM) experiments suggested that the PNA-like pattern is only possible under the tropical SST anomaly condition (Shukla and Wallace 1983; Kang and Lau 1986). Not only the mean circulation but also the variance is influenced by ENSO. For example, Renwick and Wallace (1996) argued that the occurrence of blocking in the Bering Strait region is sensitive to the averaged polarity of the PNA pattern but is even more sensitive to the phase of the ENSO cycle.

On the other hand, many studies showed that the internal atmospheric dynamical processes in the midlatitude atmosphere could generate a PNA-like pattern through the barotropic and baroclinic instability of the atmospheric mean state (Frederiksen 1983; Simmons et al. 1983). Further, Kok and Opsteegh (1985) and Held et al. (1989) stressed the role of the transient flux

* School of Ocean and Earth Science and Technology Contribution Number 6494 and International Pacific Research Center Contribution Number IPRC-296.

Corresponding author address: Dr. Soon-Il An, International Pacific Research Center, SOEST, University of Hawaii at Manoa, Honolulu, HI 96822.
E-mail: sian@hawaii.edu

anomaly in maintaining the PNA pattern. Dole and Black (1990) and Black and Dole (1993) demonstrated that the barotropic and baroclinic energy transport between the mean state and eddies could amplify the PNA pattern. Recently, Straus and Shukla (2000, 2002) analyzed winter ensemble GCM simulation, and concluded that the PNA pattern is characteristic of internal dynamics that is distinct from the ENSO-forced midlatitude circulation pattern.

Observationally, relationships between the atmospheric geopotential height anomalies and SST anomalies over the North Pacific have been investigated by Namias et al. (1988), Wallace et al. (1990, 1992), and Zhang et al. (1996, 1998), among others. Zhang et al. (1996) separated the intrinsic midlatitude air–sea coupled mode in the North Pacific [hereafter the North Pacific (NP) mode] from the ENSO-induced midlatitude coupled pattern (hereafter the ENSO mode) by removing the influence of ENSO via linear regression. However, some modeling studies (Lau and Nath 1994; Lau 1997; Saravanan 1998) asserted that it is not the structure but the strength and consistency of the midlatitude atmospheric response that are more meaningful for distinguishing ENSO and non-ENSO influences. So far, it is uncertain whether those two modes are really different, not only statistically but also physically from the observational standpoint.

In this study, we try to identify the coupled patterns of variability between midtroposphere geopotential height and SST anomalies over the tropical and North Pacific using a newly developed method called conditional maximum covariance analysis (CMCA). Our intention is to derive a coupled North Pacific pattern that is statistically unrelated to ENSO and then compare its behavior with the ENSO-forced mode. The comparison aims at identifying their differences in the context of coupled dynamics and atmospheric internal dynamics. The paper is organized as follows. Data and analysis methods are outlined in the next section. In section 3, we present CMCA results, which lead to air–sea coupled patterns over the North Pacific. In section 4, by means of lag correlation, the temporal characteristics of the ENSO and North Pacific modes that appeared in the expansion coefficients of each pattern are analyzed. Sections 5 and 6 document, respectively, the spatial signature of upper/lower atmospheric circulations and the transient activities associated with the ENSO and North Pacific modes. Section 7 discusses a puzzling relationship: the temporal concurrence between the ENSO and North Pacific modes in their 500-hPa geopotential height pattern. The last section presents a summary.

2. Data and methodology

The datasets used in this study are an ENSO index (Niño-3 index: SST anomalies averaged over 5°N–5°S, 150°–90°W), monthly mean North Pacific 500-hPa geopotential height (hereafter GPH) obtained from the National Centers for Environmental Prediction–National Center for Atmospheric Research (NCEP–NCAR) reanalysis data (Kalnay et al. 1996), and Pacific SST obtained from Reynolds (Reynolds and Smith 1994). Each dataset covers the period from 1950 to 1999.

To obtain coherent patterns between GPH and SST and to remove unwanted signals, we adopt the CMCA method (An 2003). The method is briefly discussed here.

Consider two geophysical variables, $\xi^*(\mathbf{x},t)$ and $\psi^*(\mathbf{x},t)$ that are functions of space ($\mathbf{x}$) and time (t), and a constraint time series $Z(t)$, which is a function of time only. Now, we construct two new variables $\xi(\mathbf{x},t)$ and $\psi(\mathbf{x},t)$, by removing the portions of the signals in ξ^* and ψ^* that are covariant with $Z(t)$:

$$\xi = \xi^* - Z \times \mathrm{COV}(\xi^*, \mathrm{Z})/\mathrm{VAR}(Z)/\mathrm{VAR}(Z) \quad \text{and}$$
$$\psi = \psi^* - Z \times \mathrm{COV}(\psi^*, \mathrm{Z})/\mathrm{VAR}(Z), \qquad (1)$$

where $\mathrm{COV}(x,y)$ denotes the temporal covariance between variables x and y, and $\mathrm{VAR}(z)$ denotes the variance of z. The methodology used in Eq. (1) resembles the method used in Wallace et al. (1992) and Zhang et al. (1996) for removing the signatures of ENSO.

From Eq. (1), $\mathrm{COV}(\xi,Z)$ and $\mathrm{COV}(\psi,Z)$ become zero at each spatial grid of ξ and ψ. Thus, the ξ and ψ are not correlated with Z. Using these newly defined variables, one may construct the temporal covariance matrix $\mathrm{COV}(\xi,\psi)$, whose total dimension becomes the spatial dimension of ξ by the spatial dimension of ψ. This matrix is also referred to as the "covariance matrix between ξ^* and ψ^* conditional on Z." The maximum covariance analysis [MCA; also known as singular value decomposition (SVD); Wallace et al. 1992] identifies pairs of spatial patterns that explain as much as possible of the mean-squared temporal covariance between two variables. Thus, MCA of $\mathrm{COV}(\xi,\psi)$ {hereafter MCA[$\mathrm{COV}(\xi,\psi)$] or equally the conditional MCA, $\mathrm{CMCA}(\xi^*,\psi^*;Z)$} provides coupled patterns between ξ and ψ, in which the signals related to Z have been excluded. Here, Z will be referred to as the secondary predictor.

By applying CMCA, ξ and ψ are represented by linear combinations of eigenvectors and corresponding expansion coefficients such that

$$\zeta(\mathbf{x},t) = \sum_n \alpha_n(t) e_n(\mathbf{x})$$
$$\psi(\mathbf{x},t) = \sum_m \beta_m(t) f_m(\mathbf{x}),$$

where $e_n(\mathbf{x})$ and $f_m(\mathbf{x})$ are the spatial patterns (eigenvectors) associated with ξ and ψ, respectively, and $\alpha_n(t)$ and $\beta_m(t)$ denote the expansion coefficient associated with ξ and ψ, respectively, and they are calculated by projecting ξ and ψ at a given time on each eigenvector.

3. Coherent SST and 500-hPa geopotential patterns associated with the North Pacific and ENSO modes

The first MCA mode of the GPH and SST anomalies is shown in Fig. 1, of which covariance fraction (CF) is 74% (here, CF indicates the percentage of the covariance explained by a pair of the eigenvectors to the total covariance between the two fields); the variance fraction (VF) for the SST pattern of the first MCA is 34% (VF indicates the percentage of the variance explained by the first eigenvector to the total variance), and VF for the GPH pattern is 21%. The GPH pattern resembles the PNA pattern, with a low center of action over the North Pacific near 45°N, 165°W and a high center of action over western Canada near 55°N, 120°W. The corresponding SST pattern indicates the positive SST anomalies over the Tropics, the negative SST anomalies over the central North Pacific, and the weak positive SST anomalies over the west coast of North America. The amplitude of the North Pacific SST anomalies is comparable to that of the equatorial eastern Pacific.

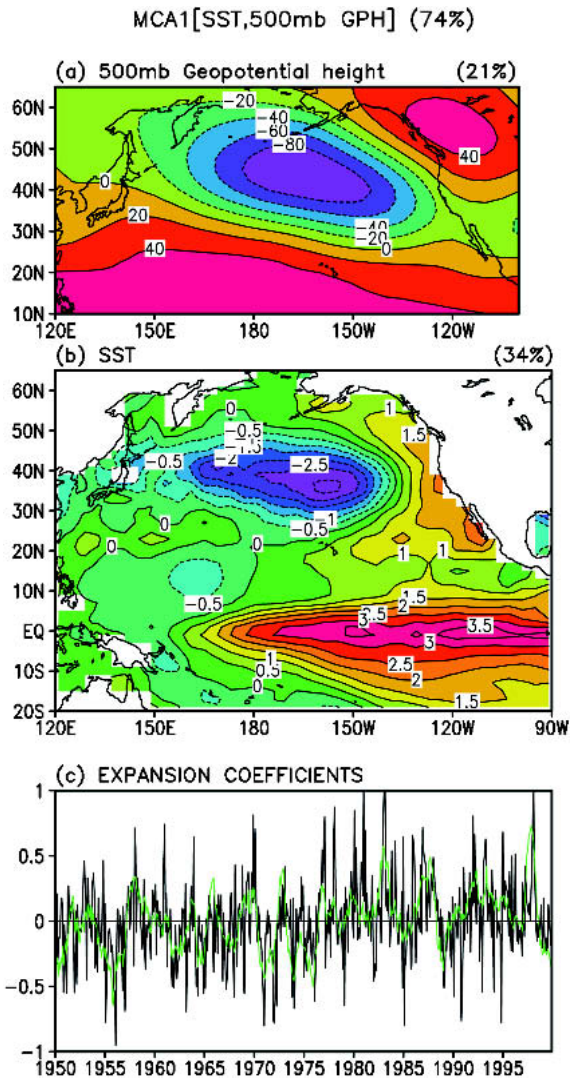

FIG. 1. Spatial patterns of the first MCA mode associated with (a) 500-hPa geopotential height and (b) SST. (c) The corresponding expansion coefficients associated with 500-hPa geopotential height (black curves) and SST (green curves). The fractions of covariance and variance of normalized data fields explained by the respective modes are indicated in the upper-right-hand corner of each map.

To obtain coherent patterns between the ocean and atmosphere that are uncorrelated with ENSO, we apply the CMCA method to the same datasets as used in the calculation in Fig. 1. In this calculation, however, the Niño-3 index (5°S–5°N, 150°–90°W) was used as the secondary predictor (the constraint condition) that corresponds to Z in Eq. (1). The CF of the first CMCA mode (Fig. 2) is 45%: the VFs for the SST and GPH pattern are 13% and 24%, respectively. The GPH pattern tends to be zonally elongated, and its center is located at 45°N, 170°W. Similar to the MCA mode shown in Fig. 1, the area of negative GPH anomalies matches that of the negative SST anomalies. Different from MCA mode, however, the ENSO-like pattern in the tropical Pacific disappears. The ENSO signal in their corresponding expansion coefficients is also not detectable. In other words, this mode has little connection with the tropical SST anomalies. This mode is almost identical to the second rotated EOF mode of Zhang et al. (1996), in which it is referred to as the "North Pacific mode." In this study we use the same name for the first CMCA mode shown in Fig. 2.

It is interesting to compare this NP mode with the SST anomaly pattern of Zhang et al. (1997). They derived the NP mode by regressing the leading principal component of the residual SST field over the Pacific domain, from which the least squares fit to the time series of the 6-yr high-pass-filtered eastern Pacific cold tongue index at each grid point has been removed (see Fig. 4 of Zhang et al. 1997). The significant difference between the NP mode (Fig. 2) and the regression pattern of Zhang et al. (1997) is found over the equatorial Pacific: the negative anomaly in NP mode and the positive anomaly in Zhang et al. (1997). Since we did not apply any filtering to the data, the large-scale tropical Pacific horseshoe pattern in Zhang et al. (1997) covering between 20°S and 20°N might be due to the low-frequency variability of the tropical SST longer than 6 yr.

To isolate the ENSO-related signatures in the North Pacific, we apply again the CMCA method to GPH and SST anomalies but with the expansion coefficients associated with the SST pattern of the NP mode (Fig. 2c) as the secondary predictor. The CF of the first CMCA mode is 70%, and VFs for SST and GPH are 38% and 15%, respectively. Clearly, the SST pattern in the tropical Pacific resembles the ENSO signature (Fig. 3b). In addition, every peak in the expansion coefficients cor-

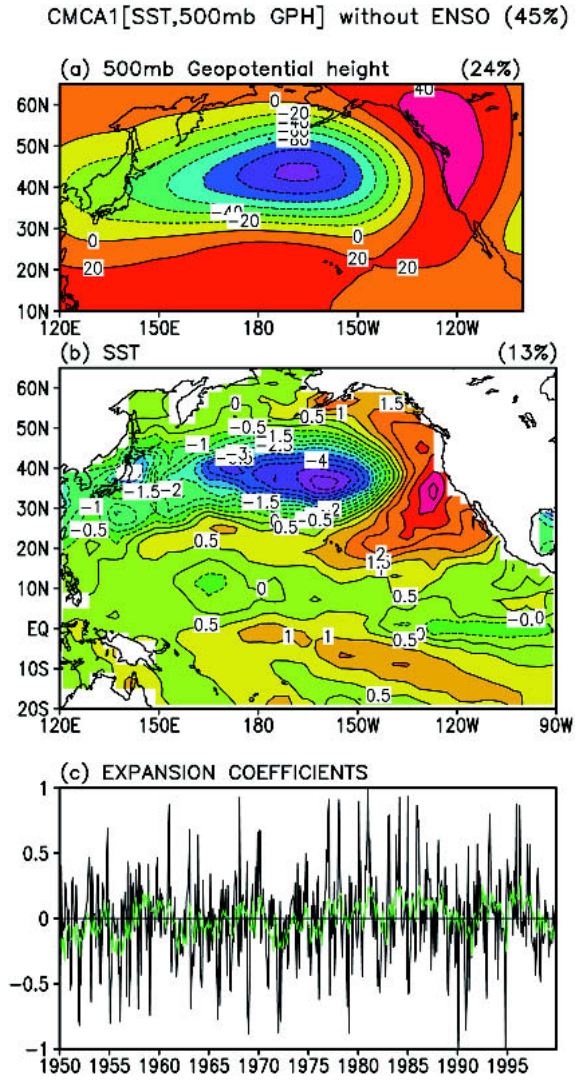

FIG. 2. As in Fig. 1 but for the spatial patterns of the NP mode derived from the leading mode of CMCA. The Niño-3 index was used as the secondary predictor.

responds to El Niño/La Niña events (Fig. 3c). Hereafter, this mode will be referred as the "ENSO mode."

The GPH anomalies associated with the ENSO mode show some subtle difference with that of the NP mode. The negative center of the GPH anomalies shifts slightly southeastward with its axis slanting toward the southeast (Fig. 3a). There is a weak ridge occurring near Japan, which is absent in the NP mode. Along this ridge, positive SST anomalies are found. In the NP mode, the SST anomalies in this region are negative. Overall, the NP and ENSO modes show a different feature in their spatial and temporal behaviors. Note that the same method was applied to, for example, both 1000- and 200-hPa GPH, and we confirmed that the correlations among the expansion coefficients associate with GPH at each level are greater than 0.9, indicating that the results are quite robust.

4. Temporal characteristics of North Pacific and ENSO modes

In this section, we investigate the differences between the NP and ENSO modes in their temporal characteristics. This is critical for understanding their physical differences.

The lagged correlation between time series of the expansion coefficients of the NP mode for SST and those for GPH (hereafter, the former refers to "NP-SST" time series and the latter refers to "NP-GPH" time series) are shown in Fig. 4 (solid line). (The dotted line in Fig. 4 corresponds to the ENSO mode; as in the NP mode, "ENSO-SST" and "ENSO-GPH" time series are defined). The positive lag indicates that GPH leads SST. As shown in Fig. 4, when the NP-GPH leads NP-

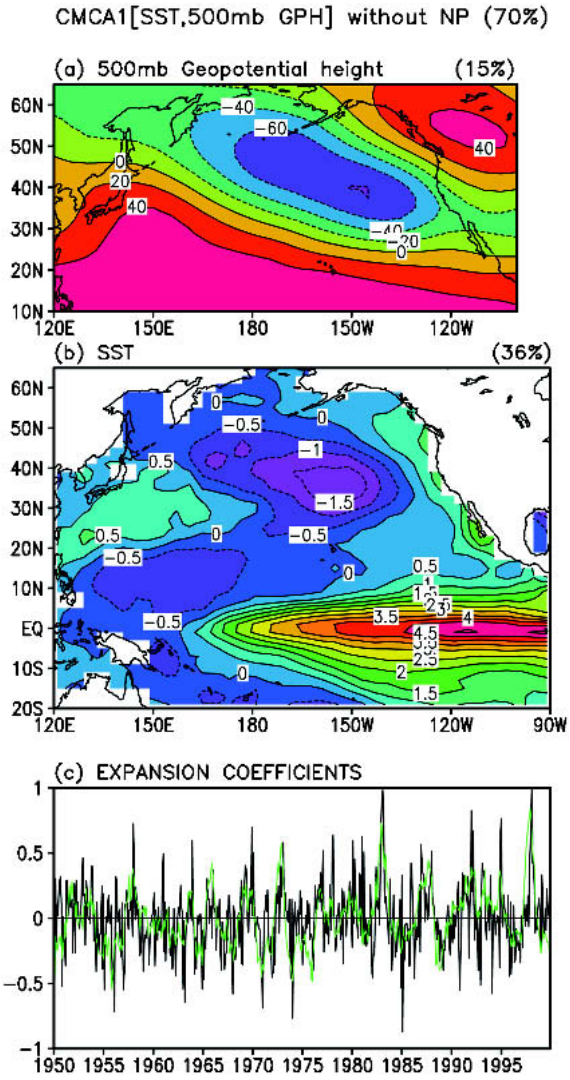

FIG. 3. As in Fig. 2 but for the ENSO mode. The time series of SST associated with the NP mode was used as the secondary predictor.

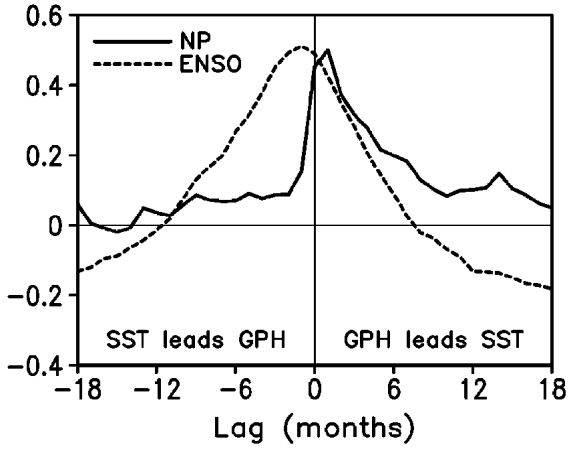

FIG. 4. Lag correlations between the time series of SST and GPH anomalies associated with the NP mode (solid) and the ENSO mode (dotted). Negative lags refer to SST leading GPH.

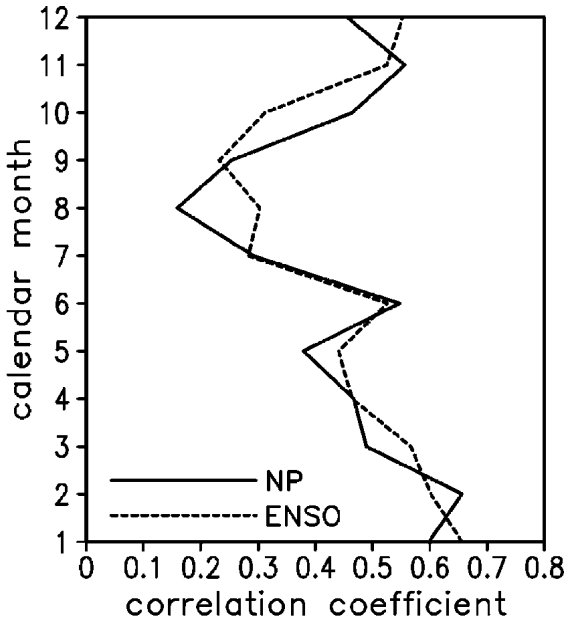

FIG. 5. Correlations between time series of SST and GPH anomalies associated with the NP mode (solid) and the ENSO mode (dotted) for a particular calendar month.

SST, the correlation is significant over a 99% confidence level from lag 0 to 4 months, while there is no significant correlation for the negative lag. The maximum positive correlation appears at a 1-month positive lag. After 1 month the lag correlation decreases slowly. It suggests that the atmosphere circulation anomalies may cause SST anomalies in the NP mode. It is known that the equivalent-barotropic low-frequency atmospheric anomaly can force the change in SST, and the atmospheric anomaly experiences a reduced surface thermal damping due to the SST adjustment as shown in AGCM experiment (Kushnir et al. 2002). The maximum correlation at a 1-month lag between NP-SST and NP-GPH may be attributed to the delayed oceanic thermal response to the atmospheric forcing, and the slow decrease of the correlation after 1 month may be related to relatively slow damping of the ocean temperature. The insignificant lag correlation for the negative lags suggests that the SST is not a major cause for changes in the atmospheric variation.

In contrast, for the ENSO mode when SST leads the GPH by 1 month the maximum correlation between ENSO-GPH and ENSO-SST occurs (Fig. 4, dotted line). Different from the NP mode, the correlation between ENSO-SST and ENSO-GPH time series gradually increases until 1 month before (-1 month lag) and then gradually decreases. This is because this ENSO mode is totally driven by the slowly varying ENSO cycle. Figure 4 suggests that NP and ENSO modes are different in terms of air–sea coupling.

Since our analysis is not for the particular season, it is unclear during which season the ocean and atmosphere are highly correlated. In Fig. 5, we further show the correlation coefficients between NP-SST time series and NP-GPH time series (solid line) for each calendar month. In general, during the late winter (January and February) the correlation is the highest, while during the late summer (July–September) the correlation is the lowest. It is known that the air–sea interaction over the North Pacific is more active during the winter (Zhang et al. 1996) as is shown in this figure. The ENSO mode (dotted line) shares the similar feature with the NP mode. Because the GPH pattern of the ENSO mode is mainly driven by the tropical SST forcing, the higher correlation during the winter is consistent with the higher SST anomaly during the winter.

To see whether there is any difference between the two modes in the predictability, we examine the persistence. The persistence indicates how long the memory of the system sustains, and hints at potential predictability of the system. Here, the persistence is defined in terms of lagged autocorrelation coefficients and the extent to which these coefficients remain at significantly high levels for extended lead times. The lag correlation of NP-SST time series and ENSO-SST time series has been calculated for each calendar month (Fig. 6). Using the correlation greater than 0.7 as a criterion for measuring the significance of the persistence, the NP mode has the most significant persistence in February–April with lead times of 3 months, while it has the least persistence in July–September (correlation falling below 0.7 after 1 month). This indicates that the signal of NP mode present in early boreal spring may persist for one season whereas that present in July–September may not persist long. This July–September persistence barrier in the NP mode is consistent with Namias and Born (1970), who showed that thermal anomalies that developed in the shallow summertime mixed layer are obliterated by vertical mixing in the next season. On the other hand, the ENSO mode starting in January–April

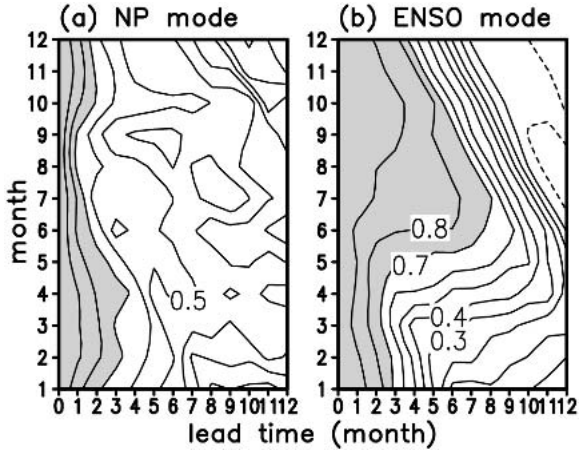

FIG. 6. Lagged autocorrelation of the time series of SST associated with (a) the NP mode and (b) the ENSO mode as a function of start month (ordinate) and lead time (abscissa). Correlations greater than 0.7 are shaded.

has the least persistence and that in June–August has the longest persistence. This seasonality leads to a well-known boreal spring persistence barrier in which correlations drop to insignificant levels during the spring season. The signal of ENSO mode present in summer and early winter will persist for two to three seasons. In summary, there is an August–September persistence barrier in the NP mode but a March–April persistence barrier in the ENSO mode.

5. Difference between North Pacific and ENSO modes in upper and lower atmospheric circulation anomalies

The linear regression maps of 200- and 1000-hPa wind vectors (zonal and meridional winds) with NP-SST time series are shown in Figs. 7a,b, respectively. Figures 7c,d are the counterparts corresponding to the ENSO mode. The correlation was calculated in the same domain as the SST pattern. The upper-level circulation associated with the NP mode (200 hPa, Fig. 7a) shows a strong westerly along the zonal band between 30° and 40°N. To the north and south of the westerly, there are easterlies. In North America, the northerly wind extends to the subtropical central Pacific, where it changes its direction to become easterly; the winds in the Tropics (20°S–10°N) are weak. On the other hand, for the ENSO mode (200 hPa, Fig. 7c), the winds over

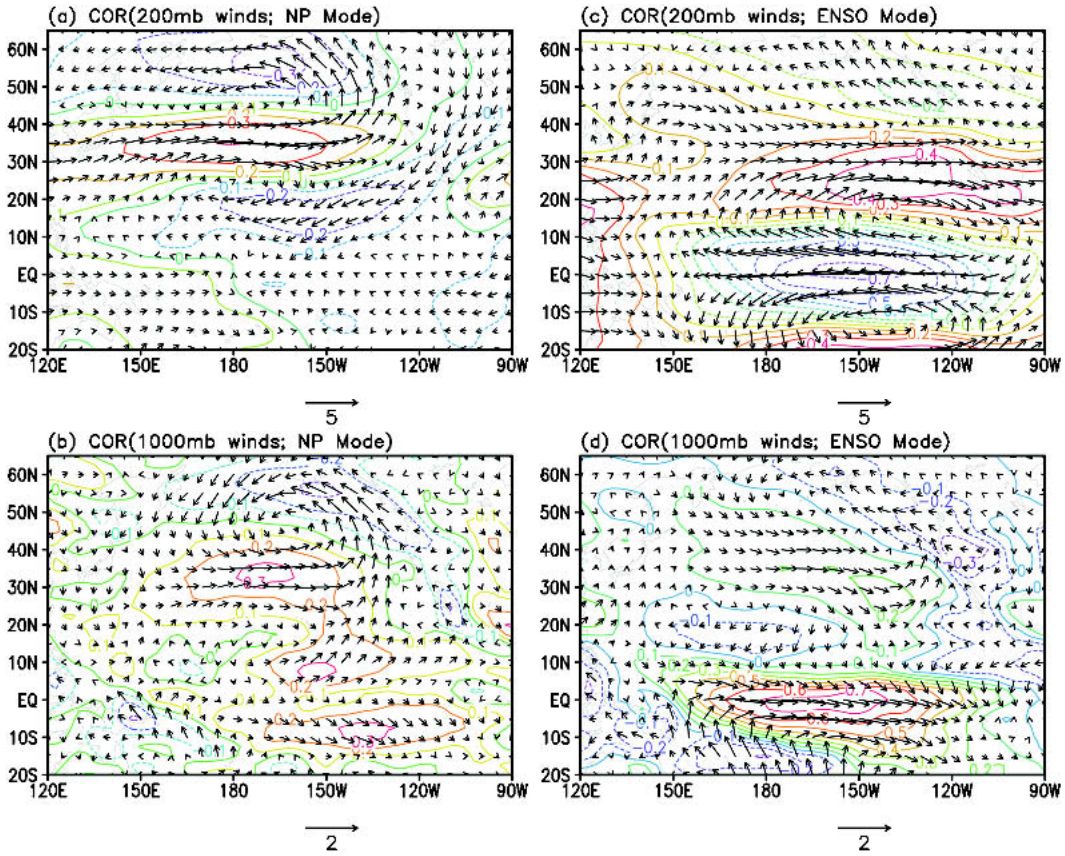

FIG. 7. (a) Linear regression map of 200-hPa winds against the time series of SST associated with the NP mode (NP-SST time series). (b) Same as (a) but for 1000-hPa winds. (c), (d) Same as in (a), (b), respectively, but for the ENSO mode. Contour indicates the correlation with the zonal wind. Unit of wind is m s^{-1}.

the midlatitude are weak; easterly winds are dominant over the tropical central and eastern Pacific, and the westerly winds prevail over the subtropical eastern Pacific.

In the lower-level circulation associated with the NP mode (1000 hPa, Fig. 7b), the strong westerly and easterly occur, respectively, between 30°–40°N and 50°–60°N. It is similar to the upper-level circulation in Fig. 7a, indicating the low-frequency barotropic response of the midlatitude atmosphere. In the subtropical northeastern Pacific, the southwesterly wind is dominant, which is in the opposite direction to the upper-level winds, indicating a baroclinic structure representing the local meridional circulation that may be due to the surface warming in the subtropical eastern coast (see Fig. 2b). The lower-level circulation of the ENSO mode (1000 hPa, Fig. 7d), on the other hand, shows a prevailing westerly over the tropical central Pacific, and thus with the upper-level easterly, it represents the weakening of Walker circulation, which is typical during El Niño. Note that the westerly in the midlatitude is not statistically significant.

In summary, both the upper- and lower-level wind patterns associated with the NP mode are basically confined to the North Pacific, whereas those associated with the ENSO mode are confined to the tropical Pacific. The upper-tropospheric jet stream associated with the NP and ENSO modes intensifies, respectively, over the central North Pacific and the subtropical northeastern Pacific.

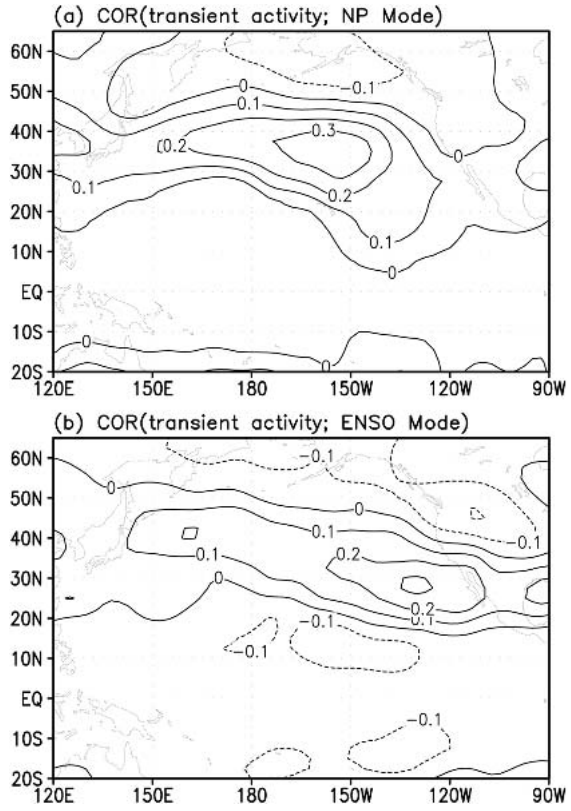

FIG. 8. (a) Correlation map of 250-hPa transient activity against the time series of SST associated with the NP mode. (b) Same as in (a) but for the ENSO mode.

6. Transient activities associated with the North Pacific and ENSO modes

The upper- and lower-level wind patterns associated with the NP and ENSO modes shown in Fig. 7 indicate monthly mean wind responses. Given the changes in these monthly mean quantities, transient fluctuations such as midlatitude weather can be modified. It was known that the midlatitude transient activities in turn influence the midlatitude mean circulation pattern (i.e., the monthly mean quantities) by providing heat and momentum flux (Held et al. 1989). However, in this section, we only focus on the changes in transient activities related to NP and ENSO modes. The transient activity in a given month, W_m is defined as

$$W_m = \sum_{n=1}^{n=N} (H_{nm} - \overline{H}_m)^2/N,$$

where H indicates the height; m and n are the indices for the month and day, respectively; N indicates the total number of days; and the overbar indicates the monthly mean. The correlation map of the transient activity at 250-hPa level against the NP-SST time series (ENSO-SST time series) is shown in Fig. 8a (Fig. 8b).

The transient activity pattern associated with the NP mode shows a maximum over the central North Pacific, which is in accord with the anomalous westerly jet exit region shown in Fig. 7a. On the other hand, the dominant positive correlation between the transient activity and ENSO-SST time series occurs in the subtropical eastern Pacific near the west coast of North America. This region corresponds to the anomalous westerly jet exit region shown in Fig. 7c. The intensification of the upper-level jet stream over the central North Pacific and the subtropical northeastern Pacific is associated with NP and ENSO modes, respectively, and in each jet exit region, the transient activities are intensified.

7. Is there a link between the North Pacific and ENSO modes?

To see whether there is any link between the NP and ENSO modes, the lag correlation between the NP-SST and ENSO-SST time series is calculated. In this correlation, a positive lag indicates that the ENSO mode leads the NP mode. As shown in Fig. 9 (solid line), when the NP mode leads the ENSO mode, the correlation is insignificant, while the correlation is significant at the 95% confidence level when ENSO leads the NP mode by 6–12 months. The gradual change in the positive lag correlation indicates that the NP mode is re-

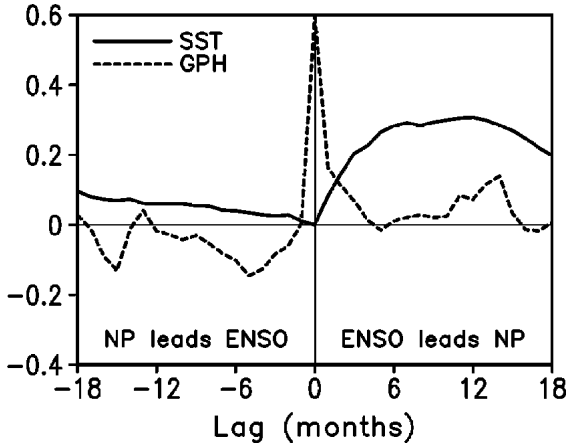

FIG. 9. Lag correlation between the NP-SST and ENSO-SST time series (solid line), and that between NP-GPH and ENSO-GPH time series (dotted line).

lated to the slowly varying part of ENSO mode in a delayed manner. It should be noted that the Niño-3 index is used as a constraint in the calculation of the NP mode, the lag correlation between NP-SST and ENSO-SST time series may be artificially affected by this constraint, resulting in zero simultaneous correlations.

The lag correlations between the NP-GPH and ENSO-GPH time series (Fig. 9, dotted line) are overall insignificant except for one peak over the 99% significance level at zero lag. This significant simultaneous correlation is expected because the GPH pattern of the NP mode (Fig. 3b) is similar to that of the ENSO mode (Fig. 2b) in many aspects. In this sense, one may argue that Fig. 9 contradicts the previous results, which showed that the NP mode differs from the ENSO mode. To resolve this dilemma, we examine their relationship in the low-frequency variability more closely. For this purpose we suppress the high-frequency variability that is contained in both the NP-GPH and ENSO-GPH time series. The idea is that the ocean tends to respond to integrated atmospheric stochastic forcing such as midlatitude weather, which results in "reddened" noise with increased power at low frequencies and decreased power at high frequencies (e.g., Frankignoul and Hasselmann 1977). We follow Newman et al. (2003), who set up a very simple model to predict the Pacific decadal oscillation (PDO) and obtained a high skill score from the model prediction. Here, the same model is adopted as

$$P_n = \alpha P_{n-1} + \xi_n, \tag{2}$$

where P is a predictand, ξ is a predictor, α is a reddening factor, and n denotes time (in months).

First, we take the normalized NP-GPH as ξ. Using Eq. (2), we calculate the value P for a given ξ, where P can be considered as a predicted SST anomaly of the NP mode. Thus, P becomes the reddened quantity of the NP-GPH time series. We perform the sensitivity test on the reddening factor α (between 0 and 1) for the same ξ. The correlation coefficients between the reddened quantities and the NP-SST time series are shown in Fig. 10 (solid line). The increase of the reddening factor results in an increase of the correlation up to 0.77, which is much higher than the original calculation (when $\alpha = 0$). On the other hand, the correlation coefficients between the reddened quantities and the ENSO-GPH time series decrease gradually to zero as α approaches 1. In other words, as the high-frequency fluctuation of GPH decreases (corresponding to increasing α), the correlation between the NP-GPH and ENSO-GPH time series becomes meaningless. It indicates that the high correlation between NP-GPH and ENSO-GPH is due to high-frequency fluctuations (e.g., shorter than interannual).

Second, we have reddened the ENSO-GPH time series (here, ξ becomes the normalized ENSO-GPH time series) and calculated the correlation between the reddened ENSO-GPH and NP-SST time series. As shown in Fig. 10 (dash–dotted line), as the reddening factor increases, the correlation also increases. However, its maximum value is below 0.3, which is far less than the correlation between the NP-GPH and NP-SST time series. In other word, the reddening of the ENSO-GPH time series cannot improve the relationship between ENSO-GPH and NP-SST, indicating that the NP mode is clearly different from the ENSO mode in this regard.

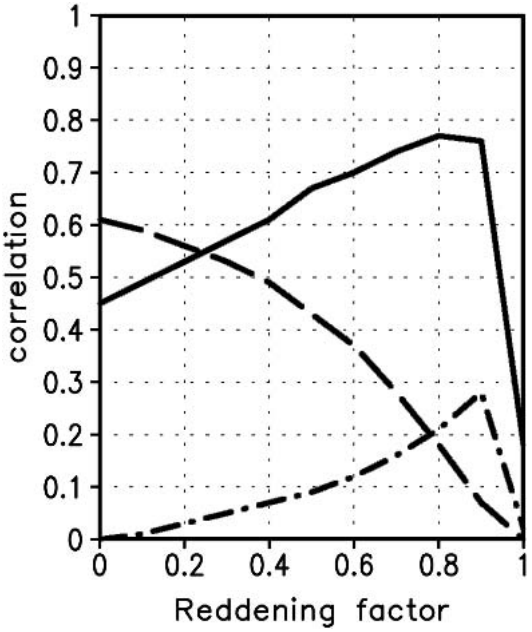

FIG. 10. Correlation between the reddened NP-GPH and the NP-SST time series as a function of the reddening factor (solid line). Dashed and dash–dotted lines indicate correlation between the reddened NP-GPH and the ENSO-GPH time series and correlation between the reddened ENSO-GPH and the NP-SST time series, respectively.

Thus, the significant simultaneous correlation between the NP-GPH and ENSO-GPH time series is surely due to the high-frequency signals that are unrelated to the corresponding SST variation.

8. Concluding remarks

Using the conditional maximum covariance analysis method, we have derived two linearly independent coupled modes between the North Pacific 500-hPa geopotential height and the SST in the tropical and North Pacific Ocean—the North Pacific (NP) and the ENSO modes. Analysis of spatial and temporal behaviors of the two modes reveals the following distinct characteristics.

1) The NP mode does not have a significant SST anomaly in the tropical Pacific; its expansion coefficient does not show any ENSO-like fluctuation.
2) The lag correlation between SST and geopotential height anomalies associated with the NP mode suggests that atmospheric changes cause the SST changes; while in the ENSO mode the tropical SST anomalies drive the atmospheric anomalies.
3) Both modes exhibit season-dependent persistence. However, the NP mode has an August–September persistence barrier, while the ENSO mode has a March–April persistence barrier.
4) The upper and lower circulation patterns associated with the NP mode show a barotropic structure that is mostly confined in the North Pacific, but those associated with the ENSO mode show a baroclinic structure that is dominant over the tropical Pacific.
5) The upper-level jet stream associated with the NP mode is intensified over the central North Pacific, while that associated with the ENSO mode is intensified over the subtropical northeastern Pacific.
6) The transient activities associated with the two modes are intensified in their corresponding jet exit regions.

Despite the above different features, the geopotential height time series associated with the two modes are significantly correlated. However, by suppressing the high-frequency variability of each time series (e.g., shorter than the interannual), this simultaneous correlation becomes insignificant, whereas the correlation between the geopotential height and SST associated with the NP mode increases. This indicates that the significant simultaneous correlation between the atmospheric anomalies of two modes is due to the coherence in the high-frequency band.

The NP mode arises from the midlatitude intrinsic atmosphere variability, while the ENSO mode originates from the Tropics. For the NP mode, the intrinsic atmospheric variability influences SST so that the atmospheric signal leads the SST, while for the ENSO mode, the midlatitude North Pacific SST anomalies are directly linked to the variations of tropical SST through atmospheric teleconnection. One possible process by which the changes in atmospheric circulation can influence SST is through changing surface heat flux (mostly due to the latent heat flux). The correlation maps of the wind speed against the SST time series associated with the NP and ENSO modes show that the cold (warm) SST region agrees with the intensification (reduction) of the wind speed, especially in the central North Pacific for the NP mode and in the equatorial central/eastern Pacific for the ENSO mode (for brevity, these figure are not shown here). Either the midlatitude storm track or Rossby wave train that originated from the Tropics is rectified by the mean flow in the midlatitudes, which may cause both effects to generate a similar SST anomaly pattern in the midlatitudes.

Acknowledgments. This study is supported by NOAA OGP through the Pacific Program and by the Japan Agency for Marine-Earth Science and Technology (JAMSTEC) through its sponsorship of the International Pacific Research Center. The authors thank Diane Henderson for editing the manuscript.

REFERENCES

An, S.-I., 2003: Conditional maximum covariance analysis and its application to the tropical Indian Ocean SST and surface wind stress anomalies. *J. Climate,* **16,** 2932–2938.

Bjerknes, J., 1969: Atmospheric teleconnections from the equatorial Pacific. *Mon. Wea. Rev.,* **97,** 163–172.

Black, R. X., and R. M. Dole, 1993: The dynamics of large-scale cyclogenesis over the North Pacific Ocean. *J. Atmos. Sci.,* **50,** 421–442.

Dole, R. M., and R. X. Black, 1990: Life cycle of persistent anomalies. Part II: The development of persistent negative height anomalies over the North Pacific Ocean. *Mon. Wea. Rev.,* **118,** 824–846.

Frankignoul, C., and K. Hasselmann, 1977: Stochastic climate models. Part II: Application to sea-surface temperature anomalies and thermocline variability. *Tellus,* **29,** 284–305.

Frederiksen, J. S., 1983: A unified three-dimensional instability theory of the onset of blocking and cyclogenesis. II. Teleconnection patterns. *J. Atmos. Sci.,* **40,** 2593–2609.

Graham, N. E., 1994: Decade-scale climate variability in the tropical and North Pacific during the 1970s and 1980s: Observations and model results. *Climate Dyn.,* **10,** 135–162.

Held, I. M., S. W. Lyons, and S. Nigam, 1989: Transients and the extratropical response to El Niño. *J. Atmos. Sci.,* **46,** 163–174.

Horel, J., and J. M. Wallace, 1981: Planetary scale atmospheric phenomena associated with the Southern Oscillation. *Mon. Wea. Rev.,* **109,** 813–829.

Hoskins, B. J., and D. Karoly, 1981: The steady, linear response of spherical atmosphere to thermal and orographic forcing. *J. Atmos. Sci.,* **38,** 1179–1196.

Kalnay, E., and Coauthors, 1996: The NCEP/NCAR 40-Year Reanalysis Project. *Bull. Amer. Meteor. Soc.,* **77,** 437–471.

Kang, I.-S., and N.-C. Lau, 1986: Principal modes of atmospheric variability in model atmospheres with and without anomalous sea surface temperature forcing in the tropical Pacific. *J. Atmos. Sci.,* **43,** 2719–2735.

Kok, C. J., and D. Opsteegh, 1985: Possible causes of anomalies in seasonal mean circulation patterns during the 1982–83 El Niño event. *J. Atmos. Sci.,* **42,** 677–694.

Kushnir, Y., W. A. Robinson, I. Blade, N. M. J. Hall, S. Peng, and

R. Sutton, 2002: Atmospheric GCM response to extratropical SST anomalies: Synthesis and evaluation. *J. Climate,* **15,** 2233–2256.

Lau, N.-C., 1997: Interactions between global SST anomalies and the midlatitude atmospheric circulation. *Bull. Amer. Meteor. Soc.,* **78,** 21–33.

——, and M. J. Nath, 1994: A modeling study of the relative roles of tropical and extratropical SST anomalies in the variability of the global atmosphere–ocean system. *J. Climate,* **7,** 1184–1207.

Namias, J., and R. M. Born, 1970: Temporal coherence in North Pacific sea-surface temperature patterns. *J. Geophys. Res.,* **75,** 5952–5955.

——, X. Yuan, and D. R. Cayan, 1988: Persistence of North Pacific sea surface temperature and atmospheric flow pattern. *J. Climate,* **1,** 682–703.

Newman, M., G. P. Compo, and M. A. Alexander, 2003: ENSO-forced variability of the Pacific decadal oscillation. *J. Climate*, **16,** 3853–3857.

Renwick, J. A., and J. M. Wallace, 1996: Relationships between North Pacific wintertime blocking, El Niño, and the PNA pattern. *Mon. Wea. Rev.,* **124,** 2071–2076.

Reynolds, R. W., and T. M. Smith, 1994: Improved global sea surface temperature analysis using optimum interpolation. *J. Climate,* **7,** 929–948.

Saravanan, R., 1998: Atmospheric low-frequency variability and its relationship to midlatitude SST variability: Studies using the NCAR climate system model. *J. Climate,* **11,** 1386–1404.

Shukla, J., and J. M. Wallace, 1983: Numerical simulation of the atmospheric response to equatorial Pacific sea surface temperature anomalies. *J. Atmos. Sci.,* **40,** 1613–1630.

Simmons, A. J., J. M. Wallace, and G. W. Branstator, 1983: Barotropic wave propagation and instability, and atmospheric teleconnection patterns. *J. Atmos. Sci.,* **40,** 1363–1392.

Straus, D. M., and J. Shukla, 2000: Distinguishing between the SST-forced variability and internal variability in mid latitudes: Analysis of observation and GCM simulations. *Quart. J. Roy. Meteor. Soc.,* **126,** 2323–2350.

——, and ——, 2002: Does ENSO force the PNA? *J. Climate,* **15,** 2340–2358.

Walker, G. T., and E. W. Bliss, 1932: World Weather V. *Mem. Roy. Meteor. Soc.,* **4,** 53–84.

Wallace, J. M., and D. S. Gutzler, 1981: Teleconnections in the geopotential height field during the Northern Hemisphere winter. *Mon. Wea. Rev.,* **109,** 784–812.

——, C. Smith, and Q. Jiang, 1990: Spatial patterns of atmosphere-ocean interaction in the northern winter. *J. Climate,* **3,** 990–998.

——, ——, and C. S. Bretherton, 1992: Singular value decomposition of wintertime sea surface temperature and 500-mb height anomalies. *J. Climate,* **5,** 561–576.

Zhang, Y., J. M. Wallace, and N. Iwasaka, 1996: Is climate variability over the North Pacific a linear response to ENSO? *J. Climate,* **9,** 1468–1478.

——, ——, and D. S. Battisti, 1997: ENSO-like interdecadal variability: 1900–93. *J. Climate,* **10,** 1004–1020.

——, J. R. Norris, and J. M. Wallace, 1998: Seasonality of large-scale atmosphere–ocean interaction over the North Pacific. *J. Climate,* **11,** 2473–2481.